The Astrophysical Journal, 945:141 (15pp), 2023 March 10 https://doi.org/10.3847/1538-4357/acbb6f
© 2023. The Author(s). Published by the American Astronomical Society.
OPEN ACCESS

Discovery of Two Polars from a Crossmatch of ZTF and the SRG/eFEDS X-Ray Catalog

Antonio C. Rodriguez[1], Shrinivas R. Kulkarni[1], Thomas A. Prince[2], Paula Szkody[3], Kevin B. Burdge[4], Ilaria Caiazzo[1], Jan van Roestel[1], Zachary P. Vanderbosch[1], Kareem El-Badry[5], Eric C. Bellm[6], Boris T. Gänsicke[7], Matthew J. Graham[1], Ashish A. Mahabal[2,8], Frank J. Masci[9], Przemek Mróz[10], Reed Riddle[11], and Ben Rusholme[9]
[1] Department of Astronomy, California Institute of Technology, 1200 E. California Boulevard, Pasadena, CA, 91125, USA; acrodrig@caltech.edu
[2] Division of Physics, Mathematics, and Astronomy, California Institute of Technology, Pasadena, CA 91125, USA
[3] Department of Astronomy, University of Washington, 3910 15th Avenue NE, Seattle, WA 98195, USA
[4] MIT-Kavli Institute for Astrophysics and Space Research, 77 Massachusetts Avenue, Cambridge, MA 02139, USA
[5] Center for Astrophysics | Harvard & Smithsonian, 60 Garden Street, Cambridge, MA 02138, USA
[6] DIRAC Institute, Department of Astronomy, University of Washington, 3910 15th Avenue NE, Seattle, WA 98195, USA
[7] Department of Physics, University of Warwick, Coventry CV4 7AL, UK
[8] Center for Data Driven Discovery, California Institute of Technology, Pasadena, CA 91125, USA
[9] IPAC, California Institute of Technology, 1200 E. California Boulevard, Pasadena, CA 91125, USA
[10] Astronomical Observatory, University of Warsaw, Al. Ujazdowskie 4, 00-478, Warszawa, Poland
[11] California Institute of Technology, Department of Astronomy, 1200 E. California Boulevard, Pasadena, CA, 91125, USA
Received 2022 June 13; revised 2023 February 10; accepted 2023 February 11; published 2023 March 15

Abstract

Magnetic cataclysmic variables (CVs) are luminous Galactic X-ray sources, which have been difficult to find in purely optical surveys due to their lack of outburst behavior. The eROSITA telescope on board the Spektr-RG mission is conducting an all-sky X-ray survey and recently released the public eROSITA Final Equatorial Depth Survey (eFEDS) catalog. We crossmatched the eFEDS catalog with photometry from the Zwicky Transient Facility and discovered two new magnetic CVs. We obtained high-cadence optical photometry and phase-resolved spectroscopy for each magnetic CV candidate and found them both to be polars. Among the newly discovered magnetic CVs is eFEDS J085037.2+044359/ZTFJ0850+0443, an eclipsing polar with orbital period $P_{\rm orb} = 1.72$ hr and WD mass $M_{\rm WD} = 0.81 \pm 0.08 M_{\odot}$. We suggest that eFEDS J085037.2+044359/ZTFJ0850+0443 is a low magnetic field strength polar, with $B_{\rm WD} \lesssim 10$ MG. We also discovered a non-eclipsing polar, eFEDS J092614.1+010558/ZTFJ0926+0105, with orbital period $P_{\rm orb} = 1.47$ hr and magnetic field strength $B_{\rm WD} = 36$–42 MG.

Unified Astronomy Thesaurus concepts: Cataclysmic variable stars (203); Binary stars (154); X-ray astronomy (1810); Time domain astronomy (2109)

1. Introduction

Magnetic cataclysmic variables (CVs) are compact object binaries in which a highly magnetized white dwarf (WD) accretes from a Roche-lobe filling donor, typically a late-type main-sequence star. Magnetic CVs are interesting for two reasons: (1) they may be the dominant contributors to the Galactic ridge hard X-ray emission (Hailey et al. 2016) and (2) the origin of the strong ($B \sim 1$–100 MG) magnetic fields in accreting WDs is uncertain (Wickramasinghe & Ferrario 2000; Schreiber et al. 2021). More broadly, they are rich laboratories for studying accretion under the influence of a strong magnetic field.

CVs typically consist of a WD accreting from a donor via an accretion disk (e.g., Warner 1995; Hellier 2001). In non-magnetic CVs, the secondary fills its Roche lobe and develops a teardrop-like shape with the tip positioned at the Lagrangian L1 point. Matter leaves the secondary star through this point and forms an accretion stream after exiting the donor star. This stream extends out until a point known as the *circularization radius*. The circularization radius is the point where the matter in the accretion stream intersects itself as it orbits the primary. The material then forms an accretion disk around the WD and makes its way to the surface through viscous dissipation of energy.

In magnetic CVs known as intermediate polars (IPs; $B_{\rm WD} \approx 1$–10 MG), the magnetic field pressure is comparable to the ram pressure of the accreted material. As a result, the disk is truncated at the Alfvén radius (also known as the magnetospheric radius). In IPs, the Alfvén radius is smaller than the circularization radius so that a partial disk forms. The accreted material initially flows through the disk but is channeled along field lines onto the WD surface inside the Alfvén radius.

In magnetic CVs known as polars ($B_{\rm WD} \gtrsim 10$ MG), the magnetic field is strong enough that the Alfvén radius is larger than the circularization radius (e.g., Hellier 2001; Mukai 2017). Matter can build up at the Alfvén radius, in a region called the stagnation region (also referred to as the threading region), before being channeled by WD magnetic field lines onto the surface (e.g., Cropper 1990; Mukai 2017).

Extensive literature and evolutionary models exist for nonmagnetic CVs (e.g., Knigge et al. 2011). In the canonical picture of nonmagnetic CVs, these systems are formed through common envelope evolution. Angular momentum loss (AML) of the binary system then drives its evolution as the WD accretes matter from its secondary companion. At orbital periods above ≈ 3 hr, magnetic braking dominates over gravitational radiation as the dominant contributor to AML. Magnetic braking is thought to shut off at the point when the donor star becomes fully convective, leading to the observed

Original content from this work may be used under the terms of the Creative Commons Attribution 4.0 licence. Any further distribution of this work must maintain attribution to the author(s) and the title of the work, journal citation and DOI.

period gap ($P_{\rm orb} \approx$ 2–3 hr). Below this gap, gravitational radiation dominates the loss of angular momentum. Few CVs have been found at orbital periods below ≈80 minutes (known as the *period bounce*), thought to correspond to the point where the donor star becomes degenerate and expands as it loses mass.

There is typically no mention of WD magnetic fields in this evolutionary model of CVs. The discovery of many magnetic CVs within the period gap, and the large number of polars, at periods below 2 hr, has led to new ideas on how magnetic CVs form and evolve (e.g., Belloni et al. 2020; Schreiber et al. 2021).

Magnetic CVs have previously been difficult to find via optical surveys alone. Both magnetic and nonmagnetic CVs have historically been discovered through their novae or dwarf novae outburst behavior. The former occurs when a thermonuclear ignition of hydrogen occurs on or near the surface of the accreting WD. The latter occurs when a thermal instability in the accretion disk leads to a temporary increase in accretion rate (Hellier 2001). However, searching via optical outbursts alone is inefficient for finding magnetic CVs. The magnetic field disrupts the disk or eliminates it entirely, which prevents thermal instability (Hameury & Lasota 2017). Novae can still occur in magnetic CVs, but are rare. As a result, optical-only surveys lead to a ∼1/100 rate of discovery for magnetic CVs (e.g., Szkody et al. 2021). However, a recent volume-limited ($d < 150$ pc) study of CVs discovered via various techniques found 36% of CVs to be magnetic (Pala et al. 2020).

Both magnetic and nonmagnetic CVs are strong X-ray emitters. The source of X-rays in magnetic CVs is typically thermal bremsstrahlung from the shock of material accreting onto the magnetic poles of the WD (e.g., Cropper 1990; Wickramasinghe & Ferrario 2000; Mukai 2017).

The source of X-rays in nonmagnetic CVs can be difficult to disentangle: the hot WD photosphere of a recent nova, the optically thick boundary layer, or accretion disk wind shock of nonmagnetic CVs can also lead to X-ray emission (Mukai 2017).

X-ray surveys help overcome the observational bias of optical-only surveys in finding CVs by uncovering both the magnetic and nonmagnetic populations (e.g., Motch et al. 1996; Bernardini et al. 2017; Halpern et al. 2018). Many magnetic CVs were discovered through the all-sky Roentgen Satellite X-ray survey (ROSAT; Truemper 1982; Voges et al. 1999; Boller et al. 2016). Hard X-ray surveys such as the Swift/BAT and INTEGRAL/IBIS surveys also led to the discovery of many CVs, primarily magnetic CVs (e.g., Mukai 2017; de Martino et al. 2020; Lutovinov et al. 2020). The ongoing eROSITA telescope on board the Spektr-RG mission (SRG; Schwope 2012; Predehl et al. 2021; Sunyaev et al. 2021) is projected to go ∼30 times deeper than ROSAT with improved localization (∼5″) of X-ray sources, guaranteeing discoveries of new magnetic CVs, among other objects, all over the sky.

In this work, we crossmatched the eROSITA Final Equatorial Depth Survey (eFEDS; Salvato et al. 2022) catalog with forced photometry of Zwicky Transient Facility (ZTF) Data Release 5 (DR5).[12] We discovered two new polars: eFEDS J085037.2+044359/ZTFJ0850+0443 and eFEDS J092614.1+010558/ZTFJ0926+0105 (henceforth ZTFJ0850+0443, and ZTFJ0926+0105, respectively). In Section 2, we present an overview of the SRG/eFEDS catalog and ZTF archival photometry. In Section 3, we outline our methodology for finding notable objects within the crossmatched data set. In Section 4, we present follow-up high-cadence photometry and spectroscopy and analyze all data for ZTFJ0850+0443. We present data and analysis for ZTFJ0926+0105 in Section 5. Finally, in Section 6, we place this work in the context of previous CV studies and discuss the utility of X-ray/optical searches for finding otherwise elusive CVs.

2. Catalog Data

2.1. eFEDS Catalog

We began with the catalog of eFEDS Galactic sources. The "Main" catalog consists of all detections detected in the 0.2–2.3 keV band with a detection likelihood larger than 6, while the "Hard" catalog consists of all sources in the 2.3–5 keV range with a detection likelihood larger than 10 (Brunner et al. 2022). Salvato et al. (2022) searched for optical counterparts to the eFEDS X-ray sources by crossmatching to the DECam Legacy Survey (DECaLS) LS8 catalog, part of the DESI Legacy Imaging Survey version DR8 (Dey et al. 2019). The mean X-ray positional error (i.e., the eROSITA/SRG uncertainty in the localization of the X-ray source) in the eFEDS catalog is 4.″7 (Salvato et al. 2022). The median separation between the X-ray source and optical counterpart, divided by the mean X-ray positional error, is 1.22 (Salvato et al. 2022). For the crossmatch to ZTF data, we use the coordinates of the LS8 optical counterpart. Given the superior depth of DECaLS (23.4 mag), we crossmatch the sources to the LS8 catalog instead of the ZTF catalog (21 mag).

Galactic sources in eFEDS are mainly identified through two methods as described in Salvato et al. (2022): (1) Sloan Digital Sky Survey (SDSS) redshifts being $z < 0.002$ and/or (2) Gaia parallaxes with good significance: $\pi/\sigma_\pi > 3$. The RUWE <1.4 can also be used. The actual method described in Salvato et al. (2022) is complex, and uses a combination of NWAY, a tool based on Bayesian statistics, and ASTROMATCH, a tool based on the maximum likelihood ratio.

In the eFEDS Main Catalog, 24774/27369 (90.5%) of X-ray sources are reported to have a reliable optical counterpart. Of those sources, 2976 are classified with the label `LIKELY GALACTIC` or `SECURE GALACTIC`. It is this sample that we further investigate with ZTF.

2.2. ZTF Data

ZTF is a photometric survey that uses a wide 47 deg^2 field-of-view camera mounted on the Samuel Oschin 48 inch telescope at the Palomar Observatory with g, r, and i filters (Bellm et al. 2019a; Graham et al. 2019; Masci et al. 2019; Dekany et al. 2020). In its first year of operations, ZTF carried out a public nightly Galactic Plane Survey in the g band and r band (Bellm et al. 2019b; Kupfer et al. 2021). This survey was in addition to the Northern Sky Survey, which operated on a 3 day cadence (Bellm et al. 2019a). Since entering Phase II, the public Northern Sky Survey is now at a 2 day cadence. The pixel size of the ZTF camera is 1″ and the median delivered image quality is 2.″0 at FWHM.

We use forced photometry from ZTF DR5. Lightcurves have a photometric precision of 0.01 mag at 13–14 mag down to a precision of 0.1–0.2 mag for the faintest objects at 20–21 mag.

[12] https://www.ztf.caltech.edu/ztf-public-releases.html

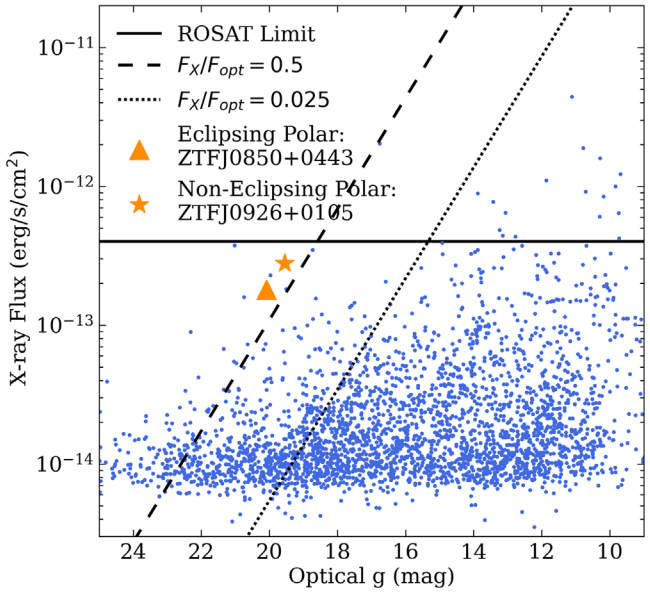

Figure 1. X-ray flux compared to DECaLS LS8 optical flux with lines of constant F_X/F_{opt} shown. All SRG/eFEDS Galactic objects are shown in blue, virtually all of which were below the detection threshold of the ROSAT All Sky X-ray Survey. The two polars stand out as systems with some of the largest F_X/F_{opt} ratios in the catalog.

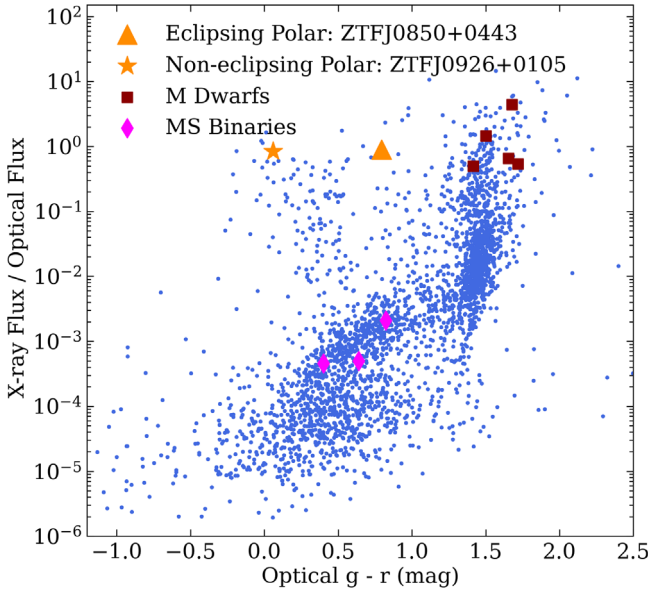

Figure 2. Ratio of X-ray flux to DECaLS LS8 optical flux as a function of optical color. The two polars cluster toward the upper left. Active M dwarfs dwarfs cluster toward the upper right and active main-sequence binaries (known as BY Dra or RS CVn) below.

While both raw photometry and forced photometry are point spread function (PSF)-fit photometry, the forced photometry calculates photometry of the object on difference images by forcing the location of the PSF to remain fixed according to the ZTF absolute astrometric reference. This allows one to obtain flux estimates below the detection threshold and therefore probe deeper than the standard photometry. For bulk download, we use a database of forced photometry files (P. Mróz & K. Burdge, et al. 2023, in preparation).

2.3. Objects of Interest

It is useful to plot the X-ray to optical flux ratio for the entire eFEDS catalog. A similar exercise has been carried out by various studies (e.g., Agüeros et al. 2009; Greiner & Richter 2015) for the ROSAT catalog and proved to be an effective way for disentangling CVs from other Galactic X-ray sources such as M dwarfs and chromospherically active binaries: BY Dra and RS CVn systems.[13] Figure 1 shows the eFEDS X-ray flux versus DECaLS LS8 optical flux plot (neither corrected for intervening Galactic absorption due to eFEDS being located outside the Galactic plane: $b > 20°$) along with ZTFJ0850+0443 and ZTFJ0926+0105. Both systems stand out as being among the systems with the highest F_X/F_{opt} ratio.

Figure 2 shows the advantage of a color cut in picking out CVs from active M dwarfs. By supplementing the X-ray to optical flux ratio with optical color information, M dwarfs cluster toward the upper right, while CVs cluster toward the upper left. The population in the lower center of the figure is generally comprised of the chromospherically and coronally active BY Dra/RS CVn systems. The labeled objects in Figure 2 have been identified through optical spectroscopy that will be presented in a follow-up study of the eFEDS field.

[13] The term BY Dra refers to chromospherically active binary stars on the main sequence, and should be distinguished from RS CVn binary stars, which are evolved and therefore above the main sequence. However, the term RS CVn has been used in the literature to refer to both; see Eker (1992) for a summary of the nomenclature.

3. Sample Selection

The goal of our study is to classify Galactic eFEDS/ZTF sources, with an emphasis on those with a high X-ray to optical flux ratio and a strong periodic signal in ZTF.

We adopt the value of optical flux, F_{opt}, for our entire study, as the standard conversion of the DECaLS LS8 g magnitude from the AB magnitude system. We assume a flat spectral energy distribution (SED) and a reference wavelength of 5000 Å. We define the following samples:

1. High X-ray to optical flux ratio. We obtain spectra for all objects with $F_X/F_{opt} > 0.5$.
2. Moderate X-ray to optical flux ratio and strong periodicity. We obtain spectra for all objects with $0.5 > F_X/F_{opt} > 0.025\%$ that feature strong periodicity and pass a color cut. Our color cut eliminates the reddest objects, which are likely to be active M dwarfs. We also report best-fit periods for the objects that do not pass the color cut.
3. Low X-ray to optical flux ratio and strong periodicity. We compile a list periods for all objects that have $F_X/F_{opt} < 0.025$.

We define the significance of periodicity as the maximum Lomb–Scargle power subtracted by the median power, all divided by the median absolute deviation. We define *strong periodicity* as lightcurves where the significance is in the 86th quantile. By this metric, approximately 10% of all objects in the eFEDS/ZTF footprint show strong periodicity. We define our color cut in the LS8 color bands and exclude objects with $g - r > 1.4$ as likely M dwarfs.

ZTFJ0850+0443 and ZTFJ0926+0105 stood out immediately from the first cut, with values of $F_X/F_{opt} > 0.5$. The Lomb–Scargle periodogram search of their lightcurves using

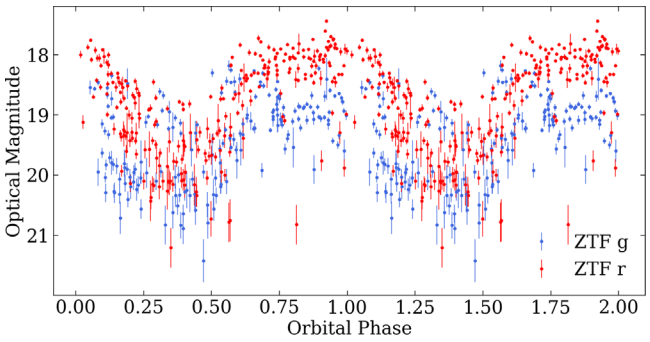

Figure 3. Folded lightcurve of ZTFJ0850+0443 (top, $P_{\rm orb} = 1.72$ hr) over ZTF forced photometry. Large amplitude variations (1–2 mag) are characteristic of cyclotron beaming in polars.

`gatspy` also showed strong periodicity (VanderPlas 2016, 2018). Both criteria prompted follow-up spectroscopy.

The full analysis of our findings from the above cuts will be reported in an upcoming study.

4. ZTFJ0850+0443

4.1. Data

ZTFJ0850+0443 was found in both ZTF *r*- and *g*-band data to be a periodic source with high amplitude. The best-fit Lomb–Scargle period is 103.44 minutes (1.72 hr) in both bands. The approximate uncertainty (in both bands) based on the frequency grid oversampling, is 0.01 minute. The folded lightcurve is shown in Figure 3. The optical position in ZTF (average FWHM: 2″) is R.A. (J2000): $08^{\rm h}50^{\rm m}37\overset{\rm s}{.}19$, decl.(J2000): $+04°\ 43'\ 57\overset{''}{.}04$, which corresponds to Gaia DR3 581892477184063232. The X-ray position in the SRG/eROSITA eFEDS catalog (positional uncertainty of source: $1\overset{''}{.}75$) is R.A. (J2000): $08^{\rm h}50^{\rm m}37\overset{\rm s}{.}22$, decl. (J2000): $+04°\ 43'\ 59\overset{''}{.}38$, which is 2″ away from the optical counterpart. No other optical or X-ray sources are present within 2″.

We followed up ZTFJ0850+0443 with high-cadence photometry in *r* and *g* bands using the Caltech HIgh-speed Multi-color camERA (CHIMERA; Harding et al. 2016) and *u* band using the Wafer-Scale Imager for Prime (WASP; Bilgi 2019). The WASP *u*-band data were only acquired over a single period, while the CHIMERA *r*- and *g*-band data were both acquired simultaneously over two orbital periods. The high-cadence data revealed the eclipse in ZTFJ0850+0443 as well as cyclotron beaming at two points during a single orbit as can be seen in Figure 4.

An identification spectrum of ZTFJ0850+0443 was acquired using the Dual Imaging Spectrograph on the 3.5 m Apache Point telescope on 2022 January 3. That spectrum revealed strong He II 4686 compared to the Hβ Balmer line. This is strong evidence of a magnetic CV, although nonmagnetic CVs can sometimes show this line behavior (Silber 1992; Oliveira et al. 2020). Additional spectra at three orbital phases were obtained on the Keck telescope using the Low-Resolution Imaging Spectrometer (LRIS; Oke et al. 1995) on 2022 February 1. A full orbit of ZTFJ0850+0443 was acquired on 2022 March 7 using LRIS. A summary of all data acquired for ZTF0850+0443 is presented in Table 1.

4.2. General Lightcurve Features

In Figure 4 we present the high-cadence photometry and spectroscopy of ZTF0850+0443 during notable orbital phases. The most prominent features of the high-cadence lightcurve are (1) the eclipse and (2) the two broad bumps per orbital phase in the *u*, *g*, and *r* bands, one of which occurs around the eclipse and the other at phase $\phi \approx 0.6$.

As described in the Introduction, the magnetic field in polars channels accreted material directly from the threading region. The material is directed by the magnetic field out of the orbital plane through the *accretion curtain* and onto the WD surface via one or two magnetic poles; see Figure 11 of Littlefield et al. (2018). Furthermore, the strong magnetic fields in polars lead to beamed cyclotron emission as nonrelativistic spiral around magnetic field lines. Cyclotron emission can manifest itself in optical lightcurves as broad 1–2 mag bumps (e.g., Cropper 1990; Hellier 2001). The data on ZTFJ0850+0443 points to it being an eclipsing polar. A visual aid to describe the system configuration is presented in Figure 5.

In most polars (≈95%), the WD spin is locked with the orbit. We searched to see if ZTFJ0850+0443 is an *asynchronous* polar (i.e., the WD spin period is not locked to the orbital period). After Gaussian smoothing of the high-cadence lightcurves, no separate WD spin period is seen, suggesting that ZTFJ0850+0443 is a (typical) tidally locked polar. Furthermore, we see no signs of a beat period (a periodogram peak above 3σ from the median) aside from the sidereal day, which could indicate a WD spin period close to the orbital period as seen in most asynchronous polars. The period obtained from the high-speed CHIMERA photometry over two orbits is the same, further suggesting against any asynchronism. For the most part, orbital periods of polars range between 1.5 and 4 hr, placing the 1.72 hr period of ZTFJ0850+0443 well within the range of most polars (e.g., Halpern et al. 2018; Abril et al. 2020; Pala et al. 2020).

In the following subsections, we walk through the orbit of ZTFJ0850+0443 and incorporate photometric and spectroscopic data to support our analysis.

4.3. Pre-eclipse

CVs, both magnetic and nonmagnetic, typically feature strong emission lines due to accretion. ZTFJ0850+0443 is now one of eight polars (Littlefield et al., 2018; C. Littlefield, private communication) where line inversions are seen in the pre-eclipse phase. Other polars that show pre-eclipse line inversions are Howell et al. (2008) and Fuchs et al. (2016). Figures 4 and 6 show that at phase $\phi = 0.93$, the H Balmer and He I lines are absorbed redward of line center. The He II 4686 line is only slightly absorbed. This also the case in the non-eclipsing polar MASTER OT J132104.04+560957.8 (Littlefield et al. 2018) as well as the eclipsing polar FL Cet (SDSS J015543.40+002807.2) (Schmidt et al. 2005). Littlefield et al. (2018) attribute this phenomenon to absorption within the accretion curtain (i.e., within the magnetosphere), not the threading region as was suspected before MASTER OT J132104.04+560957.8 was discovered. The main reason for this is that threading region is confined to the orbital plane, while the accretion curtain comes out of the plane along with the WD magnetic field lines. Since ZTFJ0850+0443 is an eclipsing system, the presence of line inversions supports the idea that this phenomenon is more common at higher

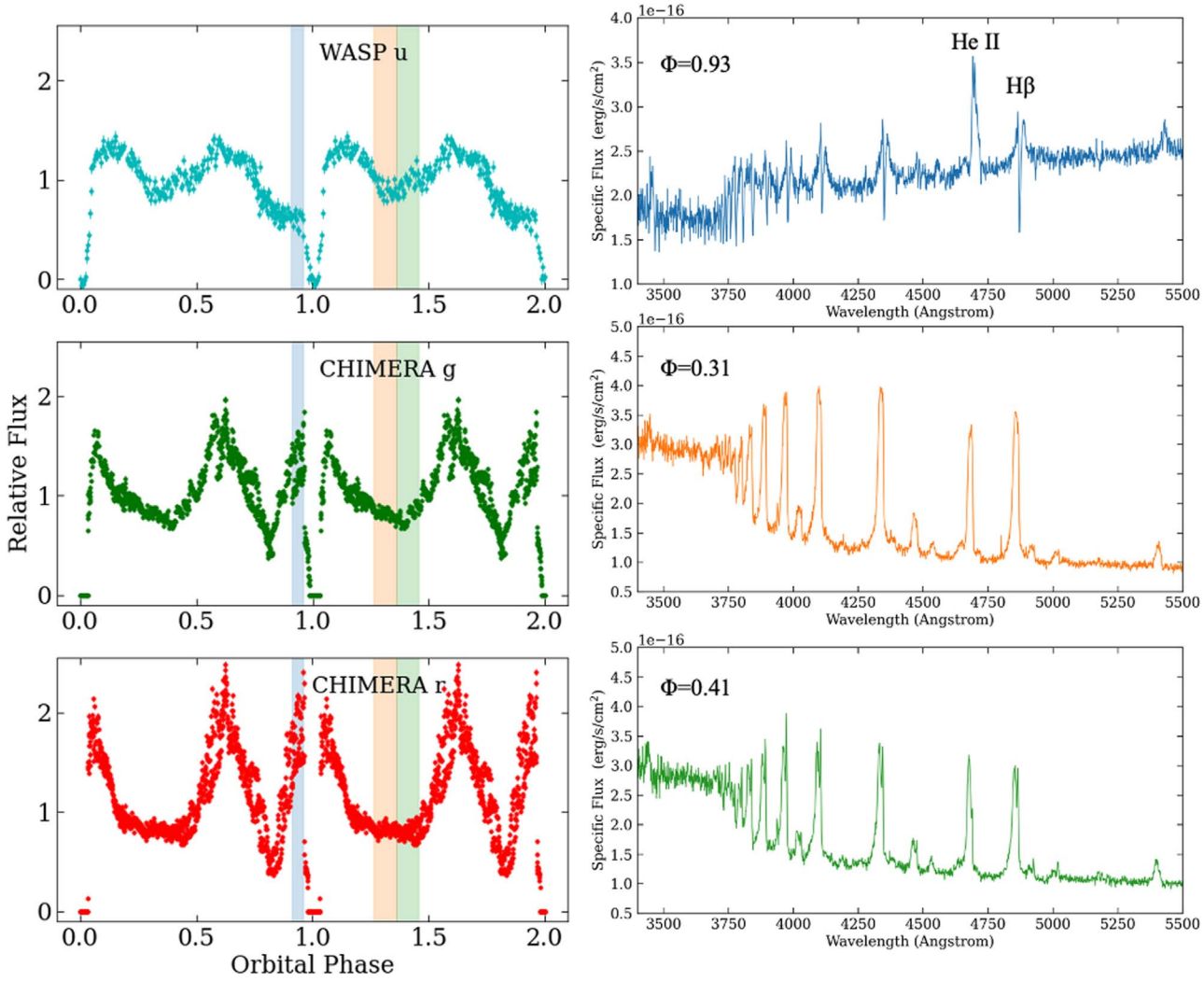

Figure 4. High-cadence photometry taken over two orbits (left) and multi-phase spectroscopy (right) of ZTFJ0850+0443. The highlights on the left panels correspond to the spectrum of the same color on the right. At phase $\phi = 0.93$, pre-eclipse line inversion is seen. At phase $\phi = 0.31$, the emission lines begin to split, revealing the irradiated face of the secondary star. At $\phi = 0.41$, the emission lines completely split and the irradiated.

inclinations ($i \rightarrow 90°$). We choose to adopt the extended *accretion curtain* as opposed to the thin *accretion column* geometry to be more general. We do not attempt to model this geometry in this study so we leave the innermost part of the accretion region as having an arbitrary width: either a curtain or a column.

Another notable feature seen at pre-eclipse is that the *u*-band flux drops while the *r*- and *g*-band flux increase (Figure 4). This is due to the *u* passband being centered blueward of the Balmer jump. In the pre-eclipse occultation of accretion spot emission by the accretion curtain, cooler material passes in front of the dominant source of radiation. Thus, the Balmer jump transitions from emission to absorption.

4.4. Eclipse: A Likely One-pole System

The lightcurve near eclipse can often be used to identify whether a polar has one or two accreting poles. We present the high-cadence lightcurve zoomed-in around the eclipse in Figure 7. The data favors ZTFJ0850+0443 being a one-pole system, but we cannot discard the possibility of a second low-luminosity accreting pole.

In the single-pole case, the pole is eclipsed at $\phi = 0.966$ as indicated by the sharp decline in the *g*- and *r*-band data. The sampling of the *u*-band data is insufficient to resolve this. The first shaded region ($\phi = 0.966$–0.988) in Figure 7 corresponds to the gradual ingress of the ballistic stream. The pole exits eclipse at $\phi = 1.033$ as indicated by the sharp rise in the *g*- and *r*-band data. The second shaded window ($\phi = 1.033$–1.05) shows the gradual egress of the accretion curtain. We denote $\phi = 1.05$ as the end of the accretion stream eclipse as that is the point where the total flux returns to its pre-eclipse value in the *r*- and *g*-band data. The *u*-band flux is larger during post-eclipse due to the absence of pre-eclipse self-absorption by the accretion curtain. Previous observations and numerical simulations have been able to reproduce remarkably similar light-curves (Breytenbach et al. 2019; Zhilkin et al. 2019).

In the case of two-pole accretion, two *steps* in the ingress and egress of the magnetic poles are often seen. However, our photometric sampling cadence (10 s) is too low to detect that. For example, a ∼0.1 s cadence was needed to see this in FL Cet (O'Donoghue et al. 2006) and a 1 s cadence for eRASSt J192932.9-560346 (Schwope et al. 2022). It could also be that the second pole is so faint at optical wavelengths that it would not appear in optical photometry at all. After all, no

Table 1
Data Acquired for ZTFJ0850+0443

Data Type	Date	Instrument	Specifications	Finding
Identification spectrum	8 Jan 2022	Apache Point 3.5 m Telescope/DIS	Blue: 3770–5030 Å, 0.75 Å resolution, 900 s exp. Red: 6200–7380 Å, 0.60 Å resolution, 900 s exp.	Strong He II indicative of magnetic nature
High-cadence *u*-band photometry	27 Jan 2022	Hale Telescope/WASP	10 s exp. for 1.8 hr	Eclipse and cyclotron beaming revealed
Multi-phase spectra	1 Feb 2022	Keck I/LRIS	Blue: 3140–5640 Å, 1.1 Å resolution, 3x900s exp. Red: 5530–8830 Å, 0.80 Å resolution, 3x900s exp.	Emission/absorption line reversals and multi-component emission
High-cadence *r* and *g*-band photometry	4 Feb 2022	Hale Telescope/CHIMERA	10 s exp. for 3.5 hr	High-cadence photometry at simultaneous orbital phases
Multi-phase spectra	7 Mar 2022	Keck I/LRIS	Blue: 3140–5640 Å, 1.1 Å resolution, 16x900s exp. Red: 5530–8830 Å, 0.80 Å resolution, 16x900s exp.	Full orbit for Doppler tomography and RVs

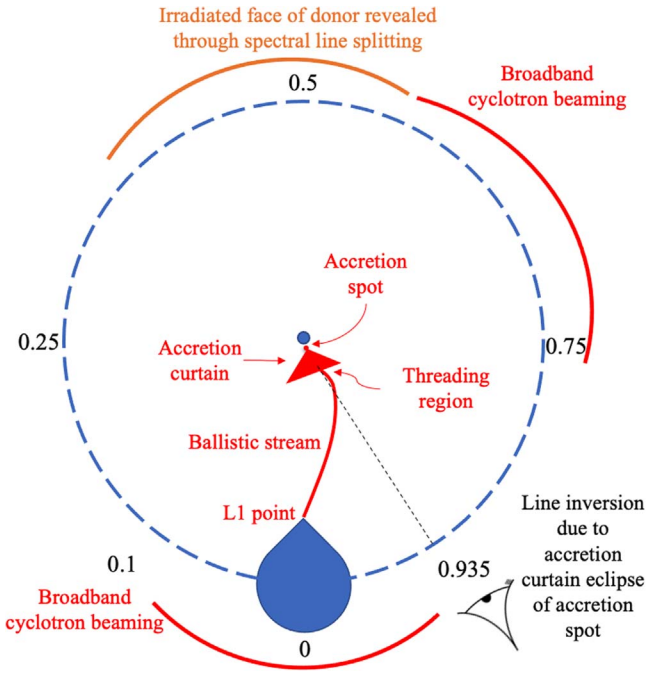

Figure 5. Cartoon of the orbit of ZTF0850+0443, based on Figure 12 of Schmidt et al. (2005). The observer can be imagined as rotating along the dashed circle as a function of orbital phase.

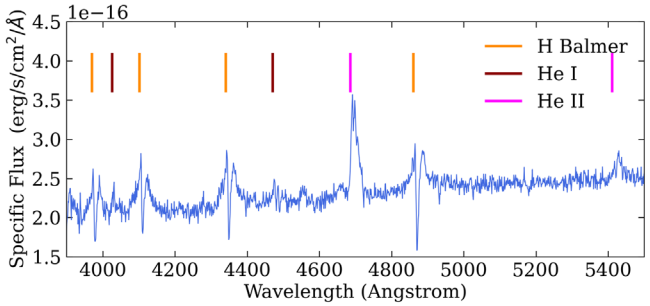

Figure 6. Zoomed-in spectrum of ZTFJ0850+0443 at $\phi = 0.93$. He II is less broad than H Balmer lines and hardly absorbed. H Balmer lines are absorbed redward of line center.

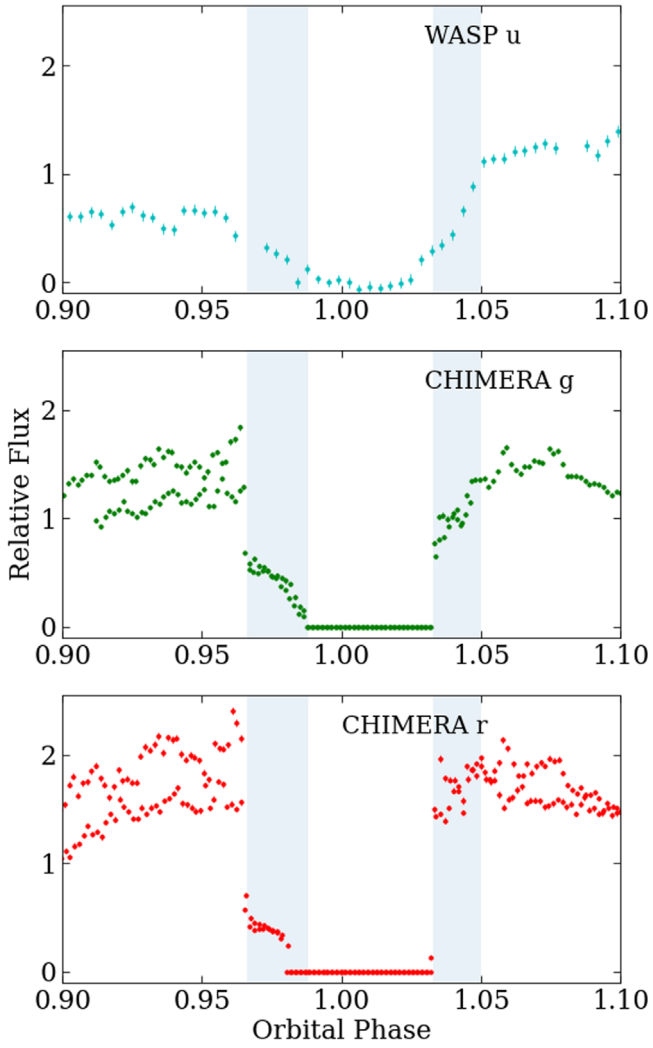

Figure 7. High-cadence lightcurve (two stacked orbits) of ZTFJ0850+0443 around the eclipse. Highlights indicate the following phases: in the one-pole accretion model, the accretion spot on the WD is eclipsed by the donor star at $\phi = 0.966$. The accretion stream is gradually eclipsed until totally disappearing at $\phi = 0.988$. The accretion spot exits eclipse at $\phi = 1.033$ and the accretion stream gradually reemerges until being fully exposed at $\phi = 1.05$.

spectroscopic evidence aside from weak evidence in the Doppler tomograms (see Section 4.6) of a second pole is seen. Additional data (e.g., optical polarimetry, X-ray lightcurves, or higher cadence optical photometry) are needed to definitively classify this as a one- or two-pole system, although the current data more strongly support the one-pole model.

On the whole, the eclipse is shallowest in the *u* band and deepest in the *r* band. This has been attributed to the accreted material being channeled in the lowest energy configuration, which concentrates cooler material toward the center of the accretion stream. Hotter material is therefore more sparse and can still be seen while the cooler, concentrated material is eclipsed (see Figure 5 of Harrop-Allin et al. 1999) for the modeling of HU Aquarii). We note that in the case of HU Aquarii, modeling of this feature alone in optical lightcurves was insufficient to determine whether the system is accreting at one or two poles.

4.5. Donor Star Revealed

At phase $\phi \approx 0.3$, the H Balmer, He I, and He II emission lines begin to split before being distinguishably separated at $\phi \approx 0.4$ (Figure 4). The broad (FWHM $\approx$ 20 Å), blueshifted component traces the accretion onto the WD. The narrow (FWHM $\approx$ 5 Å) component, which at this phase is slightly redshifted, traces the irradiated face of the donor star. At phase $\phi \approx 0.5$, the narrow component in the H Balmer, He I, and He II emission lines is at line center and stronger than the blueshifted accretion spot emission lines (Figure 8).

At this point in the orbital phase, we are seeing directly into the irradiated face of the donor, confirming the origin of the narrow emission component. This phenomenon has been known since early studies of polars (e.g., Cropper 1990) and used to constrain binary parameters of the eclipsing polar BS Tri (Kolbin et al. 2022) when the traditionally used Na I 8183, 8195 doublet could not be spotted. The Na I 8183, 8195 doublet is not seen in ZTFJ0850+0443 due to the strong accretion continuum that dominates out to red optical wavelengths. At the same orbital phases that H Balmer, He I, and He II emission lines are split into broad and narrow components (center around $\phi = 0.5$), Ca II 8498 and 8542 from

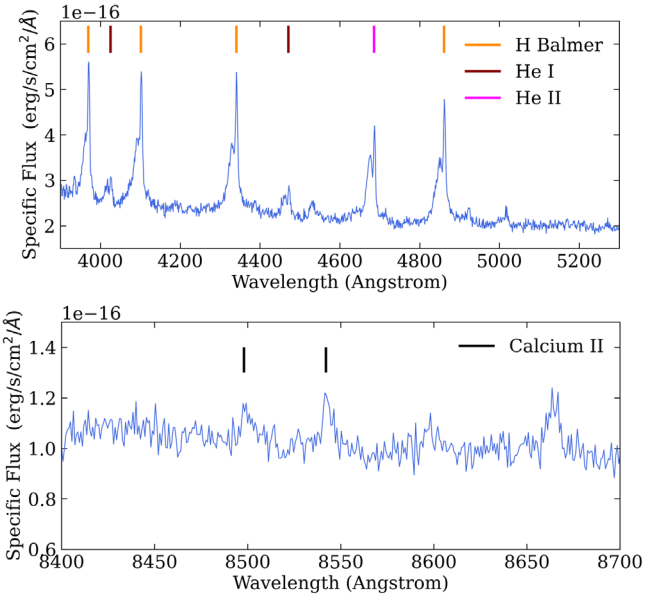

Figure 8. The narrow component of H Balmer and He I/II emission lines roughly trace the tip of the Roche lobe of the donor star (top). Ca II lines trace the irradiated face at the center of light (bottom). Spectra shown are taken near $\phi = 0.5$.

the irradiated donor are seen in emission above the accretion continuum (Figure 8).

Na I, Ca II, H Balmer, He I, and He II lines from the donor star do not all arise from the same location. The H Balmer, He I, and He II lines likely arise from the tip of the Roche lobe and possibly into the accretion stream (e.g., Schwope et al. 2011). The Ca II lines roughly trace the center of light of the irradiated donor, somewhere between the center of mass and the tip of the Roche lobe. The Na I lines tend to arise from deeper within the donor and more reliably trace the center of mass (e.g., Schwope et al. 2011). Therefore, in order to correctly use the Ca II lines to trace the radial velocity (RV) of the donor, we must apply a correction which we explain in detail in Section 4.7.

4.6. Doppler Tomography

Spectral lines in CVs vary as a function of orbital phase, often containing information about all system parameters which can be blended together. In CVs with an accretion disk, the disk, the accretion hot spot (where the accretion stream hits the disk), and irradiated face of the donor star can all contribute to the observed emission. Doppler tomography converts phase-resolved spectroscopy into a plot of observed RV and line strength as a function of orbital phase. Doppler tomograms disentangle the contribution of the various CV components (e.g., accretion disk, accretion hot spot, donor star) to a given spectral line; see Marsh (2005) for a review of the method of Doppler tomography. We present Doppler tomograms and RV curves of He II 4686 and Hβ in Figure 9.

We use the `doptomog`[14] code developed by Kotze et al. (2015). We show the *inverse* Doppler tomograms, which better illustrate the high-velocity components in magnetic CVs. Higher velocities are located closer in to the center of the diagram, while lower velocities are farther from center (traditional Doppler tomography flips this around).

[14] https://www.saao.ac.za/~ejk/doptomog/main.html

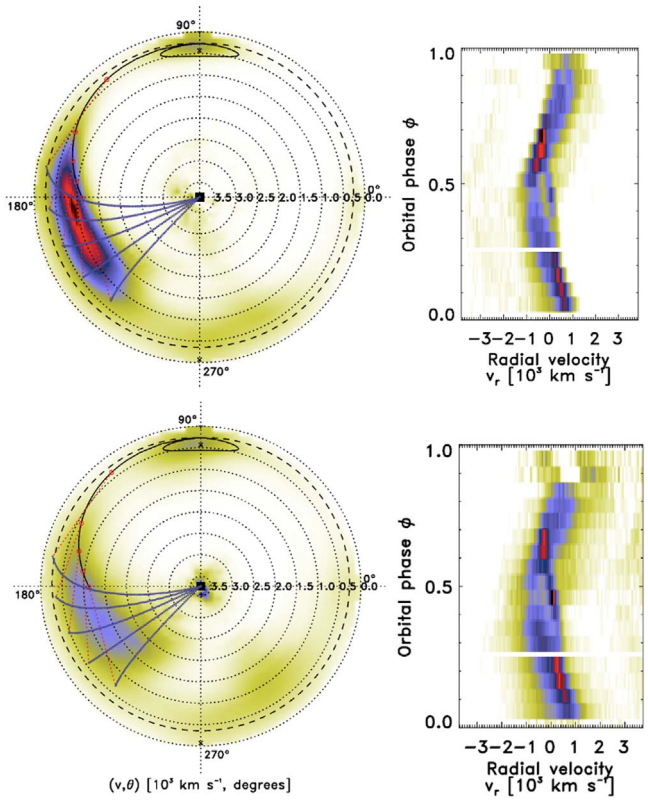

Figure 9. *Inverse* Doppler tomograms and RV curves for ZTF0850+0443 using He II 4686 (top) and Hβ (bottom). Redder color indicates stronger line strength. Model magnetic field threading is shown for clarity using generic parameters. The dominant component is that of the accretion curtain. The irradiated face of the secondary can also be seen toward the top.

The feature with an amplitude of 1000 km s^{-1} is the dominant component. The freefall velocity at the surface of a WD, assuming typical parameters ($M_{\rm WD} = 0.8 M_{\odot}$, $R_{\rm WD} = R_{\rm Earth}$) is $\approx$4000 km s^{-1}. By observing emission at 1000 km s^{-1}, we can infer that this emission is due to material within the accretion curtain as it approaches the WD surface. We do not know enough about the magnetic field configuration near the surface to know exactly where in the accretion curtain we are probing. A weak, diffuse component can also be seen toward the bottom right, which could be indicative of a second magnetic pole. This is the only possible evidence for a second pole that we have in our current data.

The irradiated face of the secondary is clearly shown roughly between 300 and 400 km s^{-1} in both Doppler tomograms as well as near $\phi = 0.5$ in the RV curves. The gap near $\phi = 0.3$ is due to a small gap in our data acquisition. The RV curves clearly show the pre-eclipse line inversion, where He II 4686 is hardly split, but Hβ is split into two components due to the intervening redshifted absorption.

4.7. Binary Parameters

In order to solve for the full mass and radius parameters of the system, we assume a circular orbit. Our constraining equations are the following: (1) the Roche lobe equation from Eggleton (1983), (2) the binary star mass function, (3) the relationship between the mass ratio and the correction applied to the RVs derived from Ca II lines, (4) an $R(M)$ relation derived from modern CV evolutionary tracks, and (5) the eclipse of the system.

The Roche lobe equation (Eggleton 1983) is

$$\frac{R_L}{a} = \frac{0.49q^{2/3}}{0.6q^{2/3} + \ln(1+q^{1/3})} = f(q), \quad (1)$$

where a is the orbital separation of the system: $a^3 = G(M_1 + M_2)P_{\rm orb}^2/4\pi^2$ and q is the ratio of the donor star mass to the WD mass: $q = M_2/M_1$. We adopt this mass ratio convention consistently throughout this study.

The binary star mass function is

$$\frac{(M_1 \sin i)^3}{(M_1 + M_2)^2} = \frac{P_{\rm orb}K_2^3}{2\pi G}, \quad (2)$$

where M_1 is the mass of the accreting WD and M_2 is the mass of the donor. K_2 is the RV of the donor, which we must infer from the observed RV of the Ca II lines, K_2'. As discussed earlier, these lines originate from the center of light of the irradiated (day) side of the donor star, which is not a good approximation for the center of mass of the donor star. We obtain $K_2' = 360 \pm 15$ km s^{-1} from a least-squares fit to the observed line profiles (Figure 11). The statistical error of 15 km s^{-1} arises from instrumental precision and low signal-to-noise in measuring the line position at certain phases. We assume the entire donor star is co-rotating around the center of mass of the system at the same orbital period. To determine the relationship between K_2 and K_2', we assume the center of light of the donor star is located $\varepsilon\, R_L$ from the center of mass of the donor star. The factor ε can be thought as being the coordinate on the axis between the donor center of mass and the tip of the Roche lobe. Therefore, the semimajor axis of the center of light is $a_2' = a_2 - \varepsilon R_L$ and the observed RV is $K_2' = 2\pi(a_2 - \varepsilon R_L)/P_{\rm orb}$. Since $K_2 = 2\pi\, a_2/P_{\rm orb}$, we can solve for the correction factor: $K_2'/K_2 = 1 - \varepsilon R_L/a_2$. Since $a = a_2(1+q)$, we write

$$\frac{K_2'}{K_2} = 1 - \varepsilon f(q) \times (1+q), \quad (3)$$

and therefore the RV correction is a function of the mass ratio $q = M_1/M2$ and ε, the coordinate on the axis between the donor center of mass and the tip of the Roche lobe. A value of $\varepsilon = 0$ corresponds to the donor center of light being located at the donor center of mass and a value of $\varepsilon = 1$ corresponds to the donor center of light being located at the tip of the Roche lobe.

In order to determine reasonable values of ε, we constructed a simple binary star model using PHOEBE (Prsa & Zwitter 2005; Prsa et al. 2016) consisting of a 15,000 K primary star (average of WDs in CVs at this orbital period, e.g., Pala et al. 2022) irradiating a 3000 K donor star at a typical CV orbital separation. This model with a single source of radiation serves as the lower limit of possible radiation for the donor. In polars, radiation from the accretion stream, accretion curtain, and accretion pole can also irradiate the donor. Modeling of the accretion-induced X-ray flux is beyond the scope of our work. However, in our simple two-star model, the center of light (location of mean intensity) at $\varepsilon = 0.45$, serves as a lower limit.

We then turn to empirical findings to place an upper limit on ε. We consider the analysis of He II, Ca II, and Na I lines of the donor star in HU Aquarii (Schwope et al. 2011). Doppler tomography of those lines showed that the Ca II lines precisely probe the center of light, located approximately at values of $\varepsilon = 0.5$–0.85.

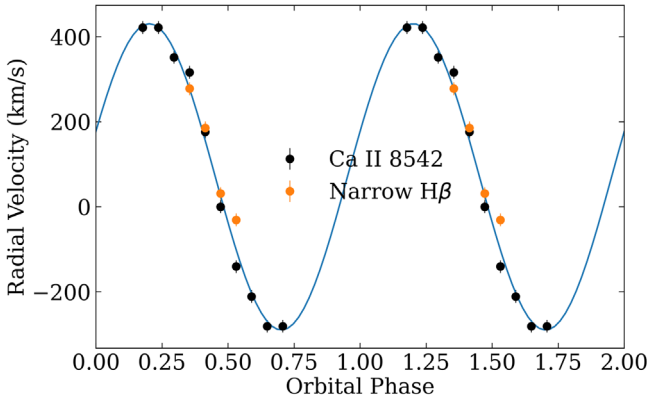

Figure 10. RV measurements of the irradiated face of the donor star as a function of orbital phases, K_2'. RV measurements are obtained at orbital phases where (1) Ca II is strong enough to be seen above the continuum or (2) the narrow component of H Balmer lines is not blended with the broad accretion component.

Therefore, we adopt the range $\varepsilon = 0.45 - 0.85$, combining the simple analytical model and empirical results. We overplot this range on our PHOEBE model in Figure 10. A full treatment of radiation from the WD, accretion spot, accretion curtain, accretion stream, and efficiency of irradiation of the donor are beyond the scope of this study.

In order to obtain an $R(M)$ relation, we use the CV donor star evolutionary tracks from the Knigge et al. (2011) set of models. They account for the inflated radius of the donor star due to the rotation it undergoes and tidal forces it experiences while in the binary system. The Knigge et al. (2011) models also account for inflation of the secondary due to irradiation by the primary.

The final component is the eclipsing nature of the system. Given the typical system parameters of polars, we know the inclination of the system must be $i \gtrsim 78°$ for the system to be eclipsing. Chanan et al. (1976) showed that if the eclipse timing is well constrained, then the mass ratio q is a function of the inclination i in Roche lobe filling systems. We find the eclipse duration to be 415 ± 5 s, measured at the sharp dropoff and sharp rise as described in Section 4.4.

The Chanan et al. (1976) geometry, however, assumes a point source located at the center of the WD and not on the surface, as is the case in polars. This however, leads to a negligible systematic that is contained within the statistic error bars on the measurement of all system parameters. Finally, we note that the deep eclipse places upper limits on the temperature of the donor star, but does not significantly tighten our final constraints on the donor star properties. The CHIMERA zero-point magnitude in the r filter is approximately 27 (Harding et al. 2016) at the time of instrument commissioning. Based on the comparison star photometry in our data, however, we estimate a zero-point magnitude of no greater than $r = 26$. At the distance of ZTFJ0850+0443 (1080^{+350}_{-250} pc), a null detection in the CHIMERA r filter places the donor star at M5 or later based on SDSS colors.

We then solve for all equations simultaneously via a vectorized least-squares approach implemented with scipy

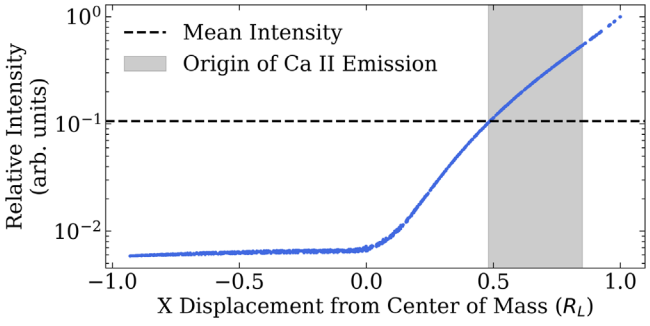

Figure 11. Output of a PHOEBE model of a late-type donor being irradiated by a 15,000 K WD. The mean intensity (center of light) is located at $\varepsilon = 0.45$, while an empirical analysis of the donor in a similar polar places the origin of Ca II emission lines to be as far away from the center of mass as $\varepsilon = 0.85$.

Table 2
System Parameters for ZTFJ0850+0443

System Parameter	Estimated Value
M_1 ($M_\odot$)	0.81 ± 0.08
M_2 ($M_\odot$)	0.119 ± 0.002
R_2 ($R_\odot$)	0.163 ± 0.002
K_2 (km s^{-1})	434 ± 15
i (degrees)	$83\overset{\circ}{.}3 \pm 1\overset{\circ}{.}2$
$P_{\rm orb}$ (hr)	1.724
$\Delta t_{\rm ecl}$ (s)	415 ± 5
$\dot{M}$ ($M_\odot$ yr^{-1})	$\sim 10^{-11}$
$\varepsilon = (a_2 - a_2')/R_L$	0.65 ± 0.20

to find the final best-fit values. This is equivalent to minimizing the error in Equation (2), Equation (3), $R_L = R(M_2)$, and the eclipse timing equation from Chanan et al. (1976) simultaneously. We present the final values for the binary system in Table 2.

The largest uncertainty in our WD mass estimate stems from the uncertainty in RV (which scales to the third power in Kepler's binary system equation). While this is limited by our estimates of the location of the donor center of light (parameterized by ε), we find that we can still reasonably constrain the mass of the WD.

4.8. Magnetic Field Strength

There are three common ways to determine the magnetic field strength of a polar as outlined by Cropper (1990): (1) cyclotron humps in the optical spectrum, (2) Zeeman splitting of emission lines in the optical spectrum, and (3) optical polarization measurements. In the case of ZTF0850+0443, we do not detect the first two and have not acquired optical polarization data to test the third criterion.

Why do we not see any cyclotron harmonics? The wavelengths of cyclotron harmonics (e.g., Ferrario et al. 2015; Mason et al. 2019) are given by the following formula:

$$\lambda_n = \frac{10710}{n}\left(\frac{100\ \mathrm{MG}}{B}\right)\sin\theta\ \text{Å}, \quad (4)$$

where λ_n is in Angstrom and θ is the viewing angle of the cyclotron beaming. In cases where cyclotron humps are seen in the optical, it is usually the $n = 3$ or $n = 4$ harmonics that are

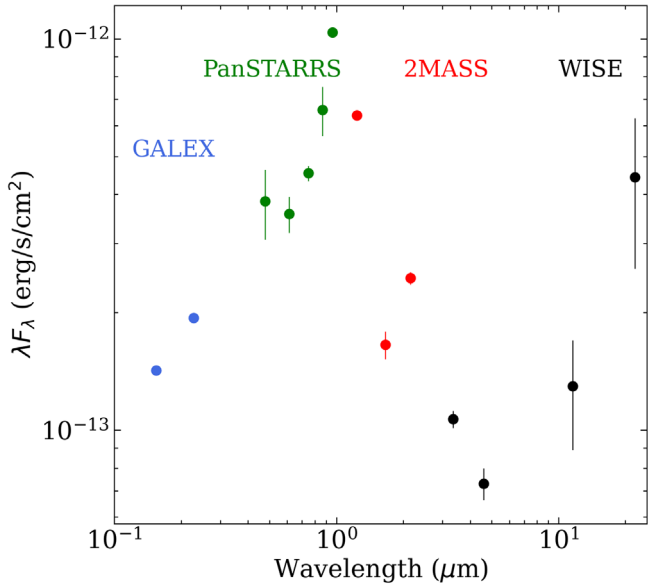

Figure 12. Extinction-corrected ($A_V = 0.19$; Schlafly & Finkbeiner 2011) SED of ZTFJ0850+0443 reproduced using average photometry from GALEX, PanSTARRS, 2MASS, and WISE data. The mid-infrared excess of ZTFJ0850+0443 suggests it is a low-field ($B \lesssim 10$ MG) polar.

seen (Cropper 1990; Wickramasinghe & Ferrario 2000). Since lower-order harmonics are less prominent, the absence of cyclotron harmonics at optical wavelengths often implies low magnetic field strength. Ferrario et al. (1993) and Wickramasinghe & Ferrario (2000) showed that in polars with field strengths of $B \lesssim 20$ MG, cyclotron harmonics ($n = 2, 3, 4$) can only be seen in near-infrared spectra and not at all in optical spectra.

When infrared spectra are not available, infrared photometry has been shown to be insightful for magnetic field characterization of low-field polars (Wickramasinghe & Ferrario 2000; Harrison & Campbell 2015). Mason et al. (2019) discovered CRTS J035010.7+323230, a polar that did not show any of the typical magnetic field diagnostics outlined by Cropper (1990). CRTS J035010.7+323230 stood out by showing a strong infrared excess with Wide-field Infrared Survey Explorer (WISE) W3 and W4 magnitudes higher than W2 and W1 points. The authors argued this was indicative of a low-field ($\lesssim$10 MG) polar. Similarly, Bernardini et al. (2019) inferred that WISE photometric excess of 2PBC J0658.01746 was indicative of a low magnetic field in a polar. We see exactly the same behavior in ZTF0850+0443, with a clear infrared excess in the WISE W3 and W4 bands. We reproduce a spectral energy distribution in Figure 12 compiled from GALEX, PanSTARRS, 2MASS, and WISE.

We propose that ZTF0850+0443 must be viewed at a high enough angle ($\sin\theta \sim 1$) from the magnetic pole so that cyclotron beaming can be observed in its optical lightcurve. What we see in the optical is likely a blend of many low-order cyclotron harmonics in the lightcurve bumps peaking at phase $\phi = 0.6$ and $\phi = 1$ (the second peak in the lightcurve would be at $\phi = 1$, but the WD is eclipsed in this system). The fundamental ($n = 1$) harmonic is then in the mid-infrared ($\sim$10–20 μm) with strong $n = 2, 3, 4$ harmonics in the near-infrared. We suggest that ZTF0850+0443 is a low-field

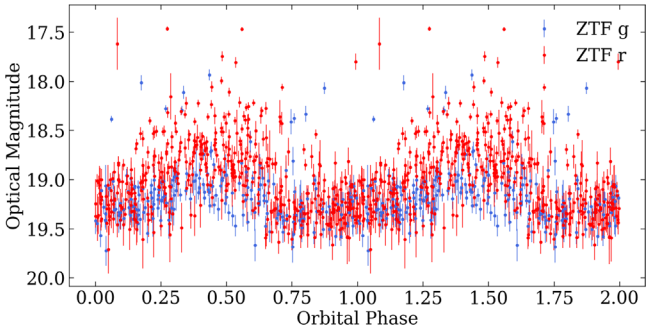

Figure 13. Folded lightcurve of ZTF0926+0105 ($P_{\rm orb} = 1.47$ hr) over ZTF forced photometry.

($B \lesssim 10$ MG) polar, potentially adding to a small pool of polars with such low magnetic field strengths.

5. ZTFJ0926+0105

5.1. Data

ZTFJ0926+0105 was found in ZTF data to be a periodic source with high amplitude in both the r and g bands (Figure 13). The optical position in ZTF (average FWHM: 2″) is R.A. (J2000): $09^{\rm h}26^{\rm m}14\overset{\rm s}{.}30$, decl. (J2000): +01° 05′ 57.″40, which corresponds to Gaia DR3 3844016380122912640. The X-ray position in the SRG/eROSITA eFEDS catalog (positional uncertainty: 1.″26) is R.A. (J2000): $09^{\rm h}26^{\rm m}14\overset{\rm s}{.}20$, decl. (J2000): +01° 05′58.″43, which is 1.″3 away from the optical counterpart. No other optical or X-ray sources are present within 2″.

We followed up ZTFJ0926+0105 with high-cadence photometry using CHIMERA. Data were acquired over 3.5 hr, but all orbital phases could not be completely covered due to transient clouds. The best-fit period of the r- and g-band data is 88.34 minutes (1.47 hr). The approximate uncertainty based on the frequency grid oversampling is 0.01 minute. Furthermore, as with ZTFJ0850+0443, we see no signs of a beat period (a periodogram peak above 3σ from the median) aside from the sidereal day, which could indicate a WD spin period close to the orbital period as seen in most asynchronous polars.

An identification spectrum was acquired using the Double Spectrograph (DBSP; Oke & Gunn 1982) on the Hale telescope on 2022 January 8. This spectrum showed strong H Balmer, He I, and He II lines in emission. He II 4686 fulfilled the criteria of Silber (1992) for being a magnetic CV candidate, prompting us to acquire follow-up spectroscopy. Phase-resolved spectra were taken on the Keck telescope using the Echelle Spectrograph and Imager (ESI; Sheinis et al. 2002) on 2022 February 1. Eight 10 minutes spectra were taken consecutively with ∼11 minutes between the starting point of each spectrum. Table 3 summarizes all data taken and the contribution of each data set.

5.2. Lightcurve and Spectral Analysis with Doppler Tomography

We see cyclotron beaming once per orbital phase in the g and r high-cadence lightcurves of ZTFJ0926+0105 (Figure 14). The large factor by which the flux increases, combined with the orbital period of 1.47 hr, is characteristic of few objects other than polars. No eclipse or any other notable features are seen. We also see a prominent cyclotron bump in the phase-resolved spectra of ZTFJ0926+0105 (Figure 14). The phase where the bump is most prominent coincides with the maximum in the photometry, confirming cyclotron beaming as the source of the high-amplitude variation. We only see one cyclotron harmonic around 8800 Å, and discuss the implications for determining the magnetic field strength in Section 5.3.

Aside from the prominent cyclotron bump, the phase-resolved spectroscopy of ZTFJ0926+0105 is much like that of ZTFJ0850+0443, revealing emission from both the accretion curtain and the face of the irradiated donor star. We produce Doppler tomograms for ZTFJ0926+0105 in order to disentangle the two components (Figure 15).

Both Doppler tomograms of ZTFJ0926+0105 reveal the irradiated face of the donor star at approximately 300 km s^{-1}, particularly the Hβ tomogram. This coincides with the presence of Ca II lines (see Figure 14), which also stem from the irradiated face of the donor star like in ZTFJ0850+0443. While we could estimate radial velocity measurements of the donor star in ZTFJ0926+0105, the lack of an eclipse prevents us from obtaining a precise estimate of the mass ratio and component masses. Both the He II 4686 and Hβ tomograms reveal large, approximately 750 km s^{-1} amplitude radial velocities. We attribute such large radial velocities to the accretion curtain, as was the case with 1000 km s^{-1} radial velocities in ZTFJ0850+0443. Since ZTFJ0926+0105 is viewed at a more face-on inclination (no eclipse is seen in the lightcurve), the observed RV should be lower.

5.3. Magnetic Field Strength

Three cyclotron harmonics are present in the spectrum of ZTFJ0926+1015 at maximum beaming ($\Phi = 0.64$ in Figure 14). We fit a polynomial continuum to the un-beamed spectrum ($\Phi = 0.78$ in Figure 14), scale it by an additive factor, and subtract it from the beamed spectrum to find cyclotron features. We find three features: a large, prominent one (180 times the continuum) peaking around 8600 Å, a smaller one (20 times the continuum) at 6450 Å, and another small one (30 time the continuum) at 5160 Å.

Using Equation (4), we must assume both a viewing angle and obtain cyclotron harmonic numbers to find the magnetic field strength. From the spacing of the three cyclotron features (8600, 6450, and 5160 Å), we deduce them to correspond to the $n = 3$, 4, 5 harmonics, respectively. There should be a $n = 6$ harmonic also present in the wavelength range of the data, but harmonics that high are usually optically thick (e.g., Cropper 1990), and the spectrum at those wavelengths is dominated by emission lines anyway. The viewing angle must also be large ($\theta \gtrsim 60°$) for the beaming to be as high amplitude as we see in the spectroscopy and photometry (e.g., Cropper 1990). We therefore adopt a viewing angle range of $\theta = 60°$–$90°$, leading to a magnetic field of $B = 36 - 42$ MG. Follow-up X-ray and optical studies could be used to determine magnetic field orientation and viewing angle of cyclotron features.

We conclude this section by presenting an SED of ZTFJ0926+0105 (Figure 16). There are no significant WISE W3 or W4 detections, consistent with ZTFJ0926+0105 having a magnetic field strength of $B = 36$–42 MG.

Table 3
Data Acquired for ZTFJ0926+0105

Data Type	Date	Instrument	Specifications	Finding
Identification spectrum	7 Jan 2022	Hale Telescope/DBSP	Blue: 3700–5870 Å, 1.5 Å resolution, 900 s exp. Red: 5700–10,200 Å, 1.1 Å resolution, 900 s exp.	Strong He II indicative of magnetic nature
High-cadence *r*- and *g*-band photometry	5 Feb 2022	Hale Telescope/CHIMERA	10 s exp. for 3.5 hr	High-cadence photometry at all orbital phases
Multi-phase spectra	6 Feb 2022	Keck II/ESI	Echelle mode: 3920–11,000 Å (not continuous); 8 × 600s exp.	Full orbit for Doppler tomography and RVs

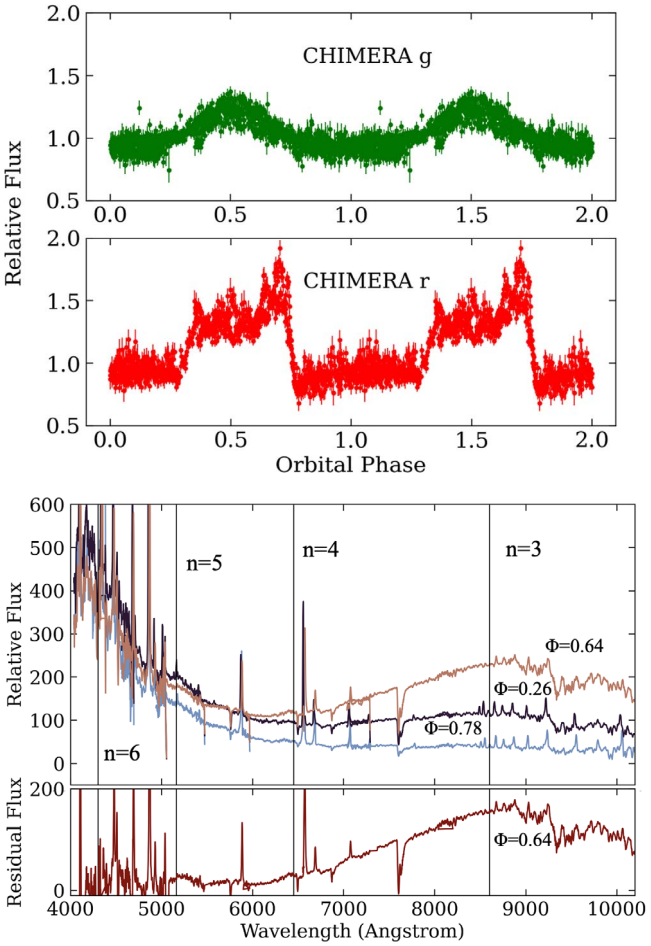

Figure 14. Cyclotron beaming is seen once per orbital phase in the high-cadence CHIMERA photometry (top) as well as phase-resolved spectroscopy (bottom).

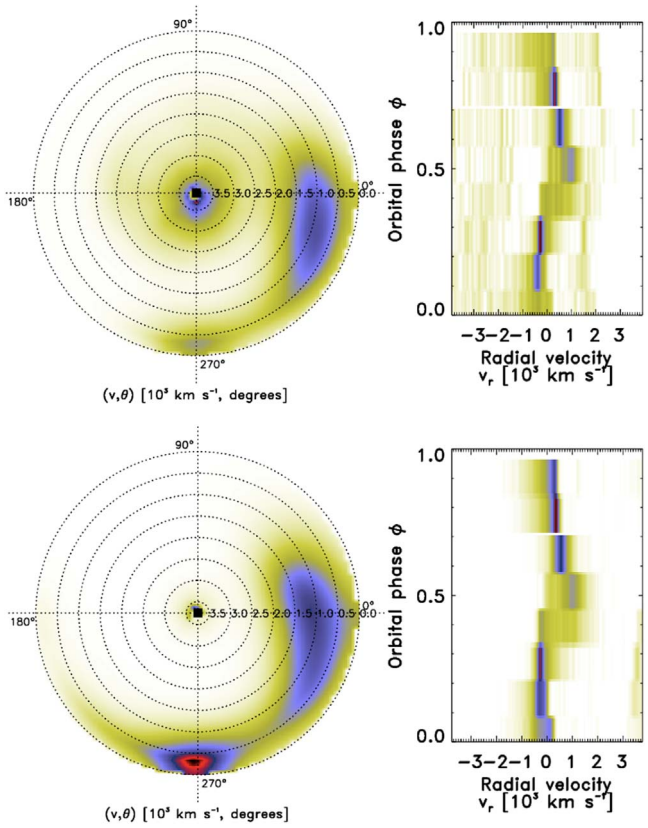

Figure 15. *Inverse* Doppler tomograms and RV curves for ZTF0926+0105 using He II 4686 (top) and Hβ (bottom). Redder color indicates stronger line strength. The dominant component is that of the accretion curtain. The irradiated face of the secondary can also be seen at the bottom, appearing stronger in Hβ compared to He II 4686.

6. Discussion

6.1. Previous Classifications and X-Ray Detections

ZTFJ0850+0443 was previously misclassified as a quasar based on its GALEX color information (Warwick et al. 2012). That same work reported a marginal XMM Slew Survey detection (with 40% flux errors), where it was listed as XMMSL1 J085036.8+044354. Had they existed at the time, Gaia proper motions or parallax would have likely prevented the misclassification.

ZTFJ0926+0105 was previously classified as a WD + M dwarf binary in Augusteijn et al. (2008) based on SDSS colors. It is likely to have been observed in a state of cyclotron beaming, during which the increase in flux at red optical wavelengths gives the impression of a late-type donor (note Figure 14 at phase $\Phi = 0.64$). ZTFJ0926+0105 is also in the Gaia WD Catalog (Gentile Fusillo et al. 2021).

6.2. Distances and X-Ray Luminosities

The Gaia EDR3 distances calculated in Bailer-Jones et al. (2021) for ZTFJ0850+0443 and ZTFJ0926+0105 are 1080^{350}_{-250} and 385^{+45}_{-40} pc, respectively.

We estimate the X-ray luminosities of ZTFJ0850+0443 and ZTFJ0926+0105 in the eROSITA Main range (0.2–2.3 keV) using the eFEDS co-added fluxes and Gaia distances. The

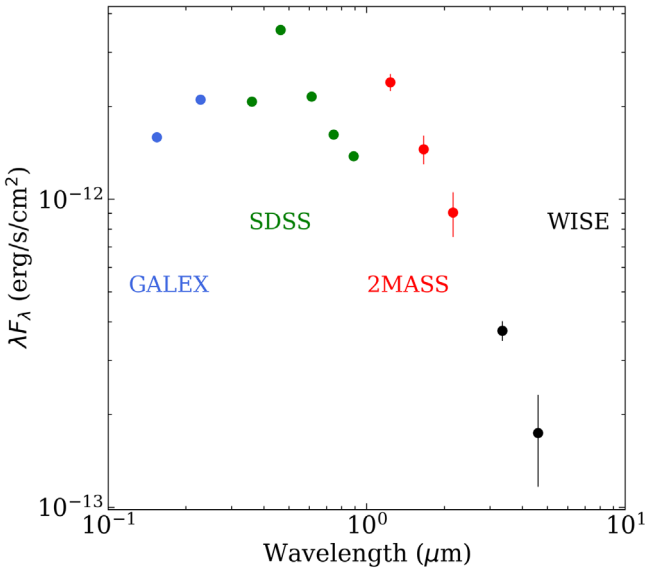

Figure 16. Extinction-corrected ($A_V = 0.12$; Schlafly & Finkbeiner 2011) SED of ZTFJ0926+0105 reproduced using average photometry from GALEX, SDSS, 2MASS, and WISE data. Unlike ZTFJ0850+0443, there is no mid-infrared excess, which could indicate this is a low-field polar.

fluxes of ZTFJ0850+0443 and ZTFJ0926+0105 are $1.80 \pm 0.16 \times 10^{-13}$ and $2.80 \pm 0.16 \times 10^{-13}$ erg s^{-1} cm^2, respectively. The X-ray luminosities (in the 0.2–2.3 keV range) of ZTFJ0850+0443 and ZTFJ0926+0105 are $2^{+2}_{-1} \times 10^{31}$

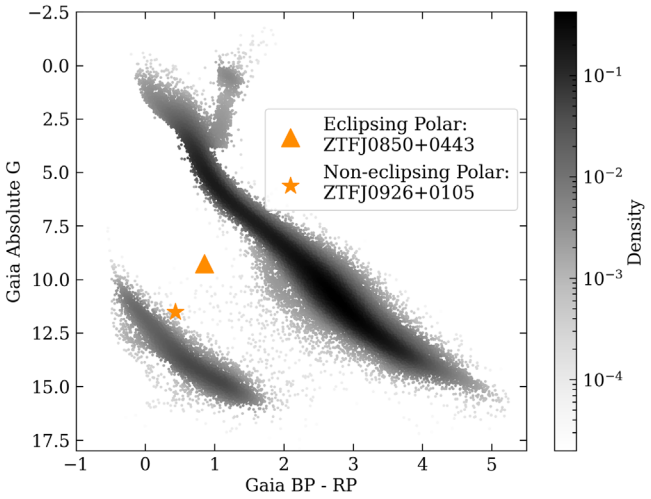

Figure 17. Gaia EDR3 HR diagram composed of sources within 100 pc with an exceptional parallax measurement ($\pi/\sigma_\pi > 10$). The two polars are located between the main sequence and WD tracks, consistent with typical polars.

erg s^{-1} and $4.7^{+1.1}_{-1.0} \times 10^{30}$ erg s^{-1}, respectively. We also note that ZTFJ0850+0443 and ZTFJ0926+0105 fulfill at least one of the criteria to be classified as X-ray variable in the eFEDS data release (Salvato et al. 2022) and are also present in the Hard (2.3–5 keV) sample.

6.3. Placement on the H–R Diagram

We overplot ZTFJ0850+0443 and ZTFJ0926+0105 (corrected for extinction) on a Gaia Hertzsprung–Russell (H–R) diagram (Figure 17). We note that ZTFJ0850+0443 has a parallax divided by parallax error (π/σ_π) value of 2.8. This is lower than the value adopted by some authors to claim a precise distance measurement ($\pi/\sigma_\pi > 3$ or even $\pi/\sigma_\pi > 10$, depending on the study). We plot all sources in Gaia EDR3 within 100 pc of the Sun with parallax $\pi/\sigma_\pi > 10$. On average, the locations of ZTFJ0850+0443 and ZTFJ0926+0105are consistent with the mean position of polars as found by Abril et al. (2020).

6.4. Current CV Population and SRG

All CVs are X-ray emitters, to some extent (Mukai 2017). While magnetic CVs typically have higher X-ray luminosities than their nonmagnetic counterparts, the eFEDS data set is deep enough to reveal new X-ray detections of nonmagnetic CVs. Even from this modest sample, the efficiency of discovery of magnetic CVs is greatly increased by incorporating X-ray data from eFEDS/SRG. Neither of the two polars were listed as SDSS CVs. A complete analysis of all CVs in the eFEDS field will be presented in a follow-up study.

An all-sky eROSITA/SRG release will be vital for constructing a volume-limited survey similar to that of Pala et al. (2020). Volume-limited samples are one way of eliminating observational bias from constructing a full picture of CVs and their evolution, as was shown by Pala et al. (2020). Introducing X-ray information eliminates another observational bias and provides another property that can be used to study CVs.

Schwope et al. (2022) identified an eclipsing polar through an eROSITA/SRG crossmatch with Gaia using a proprietary eRASS data set. We showed here that the public eFEDS data set revealed a similarly interesting object when crossmatched with ZTF.

Our findings show that the eROSITA/SRG X-ray survey is vital in supplementing ZTF for the discovery of new CVs. Making use of Gaia, we can obtain precise luminosities of the objects we find.

7. Conclusion

We have discovered two polars: ZTFJ0850+0443 (eclipsing, $P_{\rm orb} = 1.72$ hr) and ZTFJ0926+0105 (non-eclipsing, $P_{\rm orb} = 1.47$ hr), through a crossmatch of the eFEDS data set and ZTF archival photometry. We suggest that ZTFJ0850+0443 is likely a low-field polar with magnetic field $B_{\rm WD} \lesssim 10$ MG. The accreting WD in ZTFJ0850+0443 has a mass of $M_{\rm WD} = 0.81 \pm 0.08 M_\odot$, and the donor is a M5.5 dwarf typical of CV donors at short orbital periods. ZTFJ0850+0443 is now one of eight polars in the literature that shows pre-eclipse emission-line reversals, possibly due to absorption within the accretion curtain. Further study of these systems could help constrain the geometry of the accretion in polars near the central WD. Our second system, ZTFJ0926+0105, is not eclipsing, so we cannot place robust measurements on the WD mass. However, we identify cyclotron harmonics in the spectra of ZTFJ0926+0105 to determine a magnetic field strength of 36–42 MG.

This study is part of a larger follow-up analysis of the eFEDS/ZTF footprint. Studies such as this are useful in overcoming observational biases in previous optical-only searches for CVs, and will directly lead to accurate volume-limited studies of CVs such as that by Pala et al. (2020). This in turn will test our knowledge of the origin of magnetic fields in WDs, compact object accretion, and binary star evolution.

A.C.R. thanks the ZTF Variable Star Group for useful comments and discussions. A.C.R. also thanks Axel Schwope, Paul Groot, Frank Verbunt, and Jim Fuller for insightful conversations that led to an improved final manuscript. We thank Colin Littlefield for clarifying the complete census of polars with emission-line reversals in the literature. We acknowledge the staffs of the Palomar, Keck, and Apache Point observatories for their work. We thank E. Kotze for making his Doppler tomography codes public. We are grateful to the referee for useful comments and suggestions.

This work is based on observations obtained with the Samuel Oschin Telescope 48 inch and the 60 inch Telescope at the Palomar Observatory as part of the ZTF project. Major funding has been provided by the U.S National Science Foundation under grant No. AST-1440341 and by the ZTF partner institutions: the California Institute of Technology, the Oskar Klein Center, the Weizmann Institute of Science, the University of Maryland, the University of Washington, Deutsches Elektronen-Synchrotron, the University of Wisconsin-Milwaukee, and the TANGO Program of the University System of Taiwan.

The ZTF forced photometry service was funded under the Heising-Simons Foundation grant #12540303 (PI: Graham).

Some observations were made with the Apache Point 3.5 m telescope, which is owned and operated by the Astrophysical Research Corporation.

This work has made use of data from the European Space Agency (ESA) mission Gaia (https://www.cosmos.esa.int/gaia), processed by the Gaia Data Processing and Analysis

Consortium (DPAC, https://www.cosmos.esa.int/web/gaia/dpac/consortium). Funding for the DPAC has been provided by national institutions, in particular, the institutions participating in the Gaia Multilateral Agreement.

This work is based on data from eROSITA, the soft X-ray instrument aboard SRG, a joint Russian–German science mission supported by the Russian Space Agency (Roskosmos), in the interests of the Russian Academy of Sciences represented by its Space Research Institute (IKI), and the Deutsches Zentrum fr Luft- und Raumfahrt (DLR). The SRG spacecraft was built by Lavochkin Association (NPOL) and its subcontractors, and is operated by NPOL with support from the Max Planck Institute for Extraterrestrial Physics (MPE). The development and construction of the eROSITA X-ray instrument was led by MPE, with contributions from the Dr. Karl Remeis Observatory Bamberg & ECAP (FAU Erlangen-Nuernberg), the University of Hamburg Observatory, the Leibniz Institute for Astrophysics Potsdam (AIP), and the Institute for Astronomy and Astrophysics of the University of Tbingen, with the support of DLR and the Max Planck Society. The Argelander Institute for Astronomy of the University of Bonn and the Ludwig Maximilians Universität Munich also participated in the science preparation for eROSITA.

ORCID iDs

Antonio C. Rodriguez https://orcid.org/0000-0003-4189-9668
Shrinivas R. Kulkarni https://orcid.org/0000-0001-5390-8563
Thomas A. Prince https://orcid.org/0000-0002-8850-3627
Paula Szkody https://orcid.org/0000-0003-4373-7777
Kevin B. Burdge https://orcid.org/0000-0002-7226-836X
Ilaria Caiazzo https://orcid.org/0000-0002-4770-5388
Jan van Roestel https://orcid.org/0000-0002-2626-2872
Zachary P. Vanderbosch https://orcid.org/0000-0002-0853-3464
Kareem El-Badry https://orcid.org/0000-0002-6871-1752
Eric C. Bellm https://orcid.org/0000-0001-8018-5348
Boris T. Gänsicke https://orcid.org/0000-0002-2761-3005
Matthew J. Graham https://orcid.org/0000-0002-3168-0139
Ashish A. Mahabal https://orcid.org/0000-0003-2242-0244
Frank J. Masci https://orcid.org/0000-0002-8532-9395
Przemek Mróz https://orcid.org/0000-0001-7016-1692
Reed Riddle https://orcid.org/0000-0002-0387-370X
Ben Rusholme https://orcid.org/0000-0001-7648-4142

References

Abril, J., Schmidtobreick, L., Ederoclite, A., & López-Sanjuan, C. 2020, MNRAS, 492, L40
Agüeros, M. A., Anderson, S. F., Covey, K. R., et al. 2009, ApJS, 181, 444
Augusteijn, T., Greimel, R., van den Besselaar, E. J. M., Groot, P. J., & Morales-Rueda, L. 2008, A&A, 486, 843
Bailer-Jones, C. A. L., Rybizki, J., Fouesneau, M., Demleitner, M., & Andrae, R. 2021, AJ, 161, 147
Bellm, E. C., Kulkarni, S. R., Barlow, T., et al. 2019b, PASP, 131, 068003
Bellm, E. C., Kulkarni, S. R., Graham, M. J., et al. 2019a, PASP, 131, 018002
Belloni, D., Schreiber, M. R., Pala, A. F., et al. 2020, MNRAS, 491, 5717
Bernardini, F., de Martino, D., Mukai, K., et al. 2017, MNRAS, 470, 4815
Bernardini, F., de Martino, D., Mukai, K., Falanga, M., & Masetti, N. 2019, MNRAS, 489, 1044
Bilgi, P. 2019, PhD thesis, California Institute of Technology
Boller, T., Freyberg, M. J., Trümper, J., et al. 2016, A&A, 588, A103
Breytenbach, H., Buckley, D. A. H., Hakala, P., et al. 2019, MNRAS, 484, 3831
Brunner, H., Liu, T., Lamer, G., et al. 2022, A&A, 661, A1
Chanan, G. A., Middleditch, J., & Nelson, J. E. 1976, ApJ, 208, 512
Cropper, M. 1990, SSRv, 54, 195
de Martino, D., Bernardini, F., Mukai, K., Falanga, M., & Masetti, N. 2020, AdSpR, 66, 1209
Dekany, R., Smith, R. M., Riddle, R., et al. 2020, PASP, 132, 038001
Dey, A., Schlegel, D. J., Lang, D., et al. 2019, AJ, 157, 168
Eggleton, P. P. 1983, ApJ, 268, 368
Eker, Z. 1992, ApJS, 79, 481
Ferrario, L., Bailey, J., & Wickramasinghe, D. T. 1993, MNRAS, 262 285
Ferrario, L., de Martino, D., & Gänsicke, B. T. 2015, SSRv, 191, 111
Fuchs, J. T., Dunlap, B. H., Dennihy, E., et al. 2016, MNRAS, 462, 2382
Gentile Fusillo, N. P., Tremblay, P. E., Cukanovaite, E., et al. 2021, MNRAS, 508, 3877
Graham, M. J., Kulkarni, S. R., Bellm, E. C., et al. 2019, PASP, 131, 078001
Greiner, J., & Richter, G. A. 2015, A&A, 575, A42
Hailey, C. J., Mori, K., Perez, K., et al. 2016, ApJ, 826, 160
Halpern, J. P., Thorstensen, J. R., Cho, P., et al. 2018, AJ, 155, 247
Hameury, J. M., & Lasota, J. P. 2017, A&A, 602, A102
Harding, L. K., Hallinan, G., Milburn, J., et al. 2016, MNRAS, 457, 3036
Harrison, T. E., & Campbell, R. K. 2015, ApJS, 219, 32
Harrop-Allin, M. K., Cropper, M., Hakala, P. J., Hellier, C., & Ramseyer, T. 1999, MNRAS, 308, 807
Hellier, C. 2001, Cataclysmic Variable Stars (Chichester: Praxis Publishing)
Howell, S. B., Harrison, T. E., Huber, M. E., et al. 2008, AJ, 136, 2541
Knigge, C., Baraffe, I., & Patterson, J. 2011, ApJS, 194, 28
Kolbin, A. I., Borisov, N. V., Serebriakova, N. A., et al. 2022, MNRAS, 511, 20
Kotze, E. J., Potter, S. B., & McBride, V. A. 2015, A&A, 579, A77
Kupfer, T., Prince, T. A., van Roestel, J., et al. 2021, MNRAS, 505, 1254
Littlefield, C., Garnavich, P., Hoyt, T. J., & Kennedy, M. 2018, AJ, 155, 18
Lutovinov, A., Suleimanov, V., Manuel Luna, G. J., et al. 2020, NewAR, 91, 101547
Marsh, T. R. 2005, Ap&SS, 296, 403
Masci, F. J., Laher, R. R., Rusholme, B., et al. 2019, PASP, 131, 018003
Mason, P. A., Wells, N. K., Motsoaledi, M., Szkody, P., & Gonzalez, E. 2019, MNRAS, 488, 2881
Motch, C., Haberl, F., Guillout, P., et al. 1996, A&A, 307, 459
Mukai, K. 2017, PASP, 129, 062001
O'Donoghue, D., Buckley, D. A. H., Balona, L. A., et al. 2006, MNRAS, 372, 151
Oke, J. B., Cohen, J. G., Carr, M., et al. 1995, PASP, 107, 375
Oke, J. B., & Gunn, J. E. 1982, PASP, 94, 586
Oliveira, A. S., Rodrigues, C. V., Martins, M., et al. 2020, AJ, 159, 114
Pala, A. F., Gänsicke, B. T., Belloni, D., et al. 2022, MNRAS, 510, 6110
Pala, A. F., Gänsicke, B. T., Breedt, E., et al. 2020, MNRAS, 494, 3799
Predehl, P., Andritschke, R., Arefiev, V., et al. 2021, A&A, 647, A1
Prsa, A., Conroy, K. E., Horvat, M., et al. 2016, ApJS, 227, 29
Prsa, A., & Zwitter, T. 2005, ApJ, 628, 426
Salvato, M., Wolf, J., Dwelly, T., et al. 2022, A&A, 661, A3
Schlafly, E. F., & Finkbeiner, D. P. 2011, ApJ, 737, 103
Schmidt, G. D., Szkody, P., Homer, L., et al. 2005, ApJ, 620, 422
Schreiber, M. R., Belloni, D., Gänsicke, B. T., Parsons, S. G., & Zorotovic, M. 2021, NatAs, 5, 648
Schwope, A. 2012, MmSAI, 83, 844
Schwope, A., Buckley, D. A. H., Malyali, A., et al. 2022, A&A, 661, A43
Schwope, A. D., Horne, K., Steeghs, D., & Still, M. 2011, A&A, 531, A34
Sheinis, A. I., Bolte, M., Epps, H. W., et al. 2002, PASP, 114, 851
Silber, A. D. 1992, PhD thesis, Massachusetts Institute of Technology
Sunyaev, R., Arefiev, V., Babyshkin, V., et al. 2021, A&A, 656, A132
Szkody, P., Olde Loohuis, C., Koplitz, B., et al. 2021, AJ, 162, 94
Truemper, J. 1982, AdSpR, 2, 241
VanderPlas, J. 2016, gatspy: General tools for Astronomical Time Series in Python, Astrophysics Source Code Library, ascl:1610.007
VanderPlas, J. T. 2018, ApJS, 236, 16
Voges, W., Aschenbach, B., Boller, T., et al. 1999, A&A, 349, 389
Warner, B. 1995, Cataclysmic Variable Stars, Vol. 28 (Cambridge: Cambridge Univ. Press)
Warwick, R. S., Saxton, R. D., & Read, A. M. 2012, A&A, 548, A99
Wickramasinghe, D. T., & Ferrario, L. 2000, PASP, 112, 873
Zhilkin, A. G., Sobolev, A. V., Bisikalo, D. V., & Gabdeev, M. M. 2019, ARep, 63, 751